The 19th International Topical Meeting on Nuclear Reactor Thermal Hydraulics (NURETH-19) Log nr.: 19001
Brussels, Belgium, March 6 - 11, 2022

NUMERICAL SIMULATION OF THERMAL CONVECTION OVER AND THROUGH AN INTERNALLY HEATED POROUS LAYER

Victoria Hamtiaux and Miltiadis V. Papalexandris
Institute of Mechanics, Materials and Civil Engineering Université Catholique de Louvain
1348, Louvain-la-Neuve, Belgium
victoria.hamtiaux@uclouvain.be; miltos@uclouvain.be

ABSTRACT

In this work, we perform numerical simulations of natural thermal convection in a cuboidal domain that includes an internally heated porous region. The main motivation for this study comes from the need to better understand the phenomena occurring in the early stages of a loss of cooling accident in Spent Fuel Pools (SFP). In this respect, the fuel racks can be modeled as a porous medium immersed in water. Typically, in previous studies of such flows, the interstitial fluid and the solid matrix of the porous medium are assumed to be in thermal equilibrium. However, in many applications, including SFP, the validity of this assumption becomes questionable; for this reason, it is not invoked herein. The mathematical model that we employ for our simulations is based on the single-domain approach. According to it, the porosity is introduced as a field variable, thereby allowing the formulation of a single set of governing equations valid in both regions. Our study consists of direct numerical simulation of turbulent thermal convection in a domain that contains an internally heated porous region right off the bottom wall. The resulting turbulent convection in the pure-fluid region, above the porous medium, corresponds to a number of $Ra = 8.6 \times 10^5$. Herein, we provide a description of the flow structures and the temperature distribution for the two phases. Further, we present and discuss results for the turbulence statistics in the pure-fluid region.

KEYWORDS
Thermal convection, Porous medium–pure fluid domains, Thermal non-equilibrium.

1. INTRODUCTION

In this paper, we report on numerical simulations of natural thermal convection in domains with immersed porous structures. The motivation for this study comes from the urgent need for an improved understanding of the phenomena occurring during a Loss of Cooling Accident (LOCA) in spent fuel pools of nuclear power stations. After the event that occurred in Fukushima in 2011, the post-accident study commissioned by the Organisation for Economic Cooperation and Development highlighted the importance of improving our understanding of the phenomena that occur during the early stages of a LOCA [1]; with this regard, the storage racks of used fuel are macroscopically modeled as a porous medium with liquid water being the fluid.

One difficulty when treating flows in domains with an immersed porous medium is the handling of the macroscopic interface between the porous medium and the pure fluid. Most often, the presence of interfaces is numerically treated via the two-domain approach, according to which separate governing equations are prescribed for the fluid flow on the porous medium and on the pure-fluid domain [2, 3]. This approach requires the prescription of matching conditions that express the balance of forces and continuity of energy fluxes across the interface. Also, in this approach, the interface is represented as a sharp discontinuity so that the flow structures in its vicinity are not resolved.

An alternative option is the single-domain approach; see, for example [4, 5]. According to this model, the porosity is introduced as a space-varying field variable into the governing equations. This allows these equations to be simultaneously valid in both the porous and the pure-fluid regions, thereby eliminating the need to specify matching conditions at the interface. In our study, the single-domain approach has been implemented.

Also, in previous studies of flows with heat transfer in domains with superimposed pure-fluid and porous regions, it has been assumed that the fluid and the solid matrix inside the porous medium are in thermal equilibrium. Of course, in the application of spent fuel pools, the thermal-equilibrium hypothesis between the fuel racks and the surrounding water is not valid. In this case, we need two distinct energy conservation equations inside the porous region, namely one for the fluid phase and another for the solid matrix. Moreover, this allows treating the solid matrix as internally heated by adding a heat source term in its energy conservation equation.

2. GOVERNING EQUATIONS AND NUMERICAL ASPECTS

Let Ω be a domain consisting of a porous region Ω_p and a surrounding pure-fluid region Ω_f. Also, let S_Ω denote the boundary between the porous and pure-fluid regions. The porosity ϕ is introduced as a field variable measuring the density of volume occupied by the fluid and varies in space $\phi(\mathbf{x})$. As such, $\phi(\mathbf{x}) < 1$ for $\mathbf{x} \in \Omega_\mathrm{p}$ while $\phi(\mathbf{x}) = 1$ for $\mathbf{x} \in \Omega_\mathrm{f}$. The axiomatic definition of porosity can be found, for example, in [6, 7]. The solid matrix of the porous medium is assumed to be rigid, with constant density and zero velocity. Also, it is heated internally and therefore acts as a source of energy. Moreover, the fluid phase is assumed to be a single Newtonian and isotropic fluid substance. Besides, the two co-existing phases in the porous region Ω_p are assumed to be at thermal non-equilibrium with each other. According to the low-Mach number approximation of the thermo-mechanical model [8], the mass, momentum, and energy balance laws for the fluid phase, as well as the energy balance law for the solid skeleton reads, respectively in dimensionless form,

$$\phi\frac{\partial\rho}{\partial t} + \nabla\cdot(\phi\rho\mathbf{u}) = 0\,, \tag{1}$$

$$\phi\rho\frac{\mathrm{d}\mathbf{u}}{\mathrm{d}t} + \phi\nabla p = \frac{1}{Re}\nabla\cdot(\phi\mu\mathbf{V}) - \phi\rho Ri\tilde{\mathbf{y}} - \boldsymbol{\delta}\,\mathbf{u}\,, \tag{2}$$

$$\phi\rho c_p\frac{\mathrm{d}T}{\mathrm{d}t} - \phi\frac{\gamma-1}{\gamma}\frac{\partial p^0}{\partial t} = \frac{1}{Pr\,Re}\nabla\cdot(\phi k\nabla T) + \tilde{h}(T_\mathrm{s}-T)\,, \tag{3}$$

$$(1-\phi)\rho_\mathrm{s}c_{ps}\frac{\mathrm{d}T_\mathrm{s}}{\mathrm{d}t} = \frac{1}{Pr\,Re}\nabla\cdot(1-\phi)\mathbf{k}_\mathrm{s}\nabla T_\mathrm{s} - \tilde{h}(T_\mathrm{s}-T) + r\,. \tag{4}$$

In the above system, $\frac{\mathrm{d}}{\mathrm{d}t}$ represents the material derivative of a given quantity and $\tilde{\mathbf{y}}$ is the unit vector in the normal direction. Also, following standard notation, ρ, $\mathbf{u} = (u, v, w)$, and T denote, respectively, the fluid's density, velocity vector, and temperature. Additionally, p^0 stands for the fluid's thermodynamic pressure and p for the sum of the fluid's dynamic pressure and bulk viscous pressure [9]. It is noted that p^0 is function of time only, i.e., $p^0 = p^0(t)$ [8]. Moreover, ρ_s and T_s denote the density and temperature of the solid matrix, respectively, and γ denotes the Poisson's ratio.

In equation (2), $\mathbf{V}$ represents the deviatoric part of the viscous stress tensor, and $\boldsymbol{\delta}$ the drag force between the fluid and the solid phase. In general, the solid matrix is an anisotropic medium and, therefore, $\boldsymbol{\delta}$ is a second-order tensor. The term $\tilde{h}(T_\mathrm{s} - T)$ in the energy equations (3) and (4) represents the interphasial heat transfer, with $\tilde{h}$ being the corresponding coefficient. Also, r represents the heat-source term of the

solid matrix. Finally, c_p, k, and μ are, respectively, the fluid's heat capacity, thermal conductivity, and shear viscosity, whereas c_{ps} and $\mathbf{k}_s$ stand for the heat capacity and the thermal conductivity of the solid matrix. Since, in general, the solid matrix is anisotropic, $\mathbf{k}_s$ is a second-order tensor as well.

The dimensionless groups that arise in these equations are the Reynolds, Richardson, and Prandtl numbers,

$$Re \;=\; \frac{\hat{u}_r \hat{h}_r}{\hat{\nu}_r}\,, \qquad Ri \;=\; \frac{\hat{g}}{\hat{h}_r \hat{u}_r^2}\,, \qquad Pr = \frac{\hat{\nu}_r}{\hat{\alpha}_r}\,, \tag{5}$$

where $\hat{u}_r$ is the characteristic velocity, $\hat{h}_r$ the characteristic length, $\hat{\nu}_r$ the reference kinematic viscosity, $\hat{\alpha}_r$ the reference thermal diffusivity and $\hat{g}$ the gravitational acceleration. Dimensional variables are denoted with the hat symbol $(\hat{\cdot})$ throughout this work.

The governing system (1)–(4) is closed with an appropriate equation of state for the working fluid. Since in our study, this is liquid water, we employ an "isobaric equation of state" which gives the variation of density with temperature. This equation is a fourth-order polynomial fit of the tabulated data in [10] for water density at one atmosphere and over the temperature range of interest. The other liquid properties k, c_p and μ are also calculated via a fourth-order polynomial fit of data taken from [10].

Concerning the microstructure of the porous medium, we consider an orthotropic medium whose porosity ϕ is uniform and equal to 0.6. Also, the solid matrix is assumed to be composed of identical and uniformly distributed circular cylinders which are parallel to each other and the side walls. As regards $\boldsymbol{\delta}$ and $\mathbf{k}_s$, the transport parameters involved in the interaction between the solid matrix and the surrounding fluid are diagonal second-order tensors because this medium is orthotropic. Moreover, the coefficients in the horizontal (x and z) directions are equal, i.e., $\delta_{11} \;=\; \delta_{33}$ and $k_{s11} \;=\; k_{s33}$.

The vertical cylindrical elements that comprise the solid matrix are considered to be made of stainless steel. Each cylinder being apart from the others, we consider no conductive heat transfer in the horizontal directions as a first approximation, i.e. $k_{s11} = 0 = k_{s33}$. Then $k_{s22} = k_s$ where k_s is the non-dimensional thermal conductivity of stainless steel.

With regard to the interphasial drag coefficients δ_{11} and δ_{33}, they can be approximated as follows [11]. We consider the expression for the drag force per unit length $\hat{F}$ induced by the 2D flow around a single cylinder at low Reynolds number proposed in [12]

$$\hat{F} \;=\; \hat{\mu}\,\left(k_0 + k_2 * Re_{d_c}^2\right)\,\hat{u}\,, \tag{6}$$

where Re_{d_c} corresponds to the Reynolds number based on the diameter of a single cylinder $\hat{d}_c$ and the local velocity. This diameter also refers to the reference length of the microstructure. Then we multiply the above expression by the height of the porous medium $\hat{h}_p$ and by the number density $\hat{N}_c$ of the cylinders,

$$\hat{N}_c \;=\; \frac{4(1-\phi)}{\pi \hat{d}_c^2 \hat{h}_p}\,, \tag{7}$$

After the non-dimensionalization, the final expression reads,

$$\delta_{11} \;=\; \delta_{33} \;=\; \frac{1}{Re}\frac{4\mu}{\pi}\frac{(1-\phi)}{d_c^2}\left(k_0 + k_2 * Re_{d_c}^2\right)\,, \tag{8}$$

where Re is the macroscopic Reynolds number, $\mu = \hat{\mu}/\hat{\mu}_r$ is the dimensionless fluid viscosity and $d_c = \hat{d}_c/\hat{h}_r$ is the dimensionless diameter of a single cylinder.

For the derivation of the expression of the component δ_{22} of $\boldsymbol{\delta}$, we consider the skin-friction drag for flow over a flat plate and over a distance equal to the height of the porous medium $h_{\rm p}$. This value is then multiplied by the perimeter of one cylinder and the number density of cylinders. This results in the following non-dimensional expression [5],

$$\delta_{22} \;=\; \frac{2.656}{\sqrt{Re}}\frac{(1-\phi)}{d_{\rm c}}\sqrt{\frac{\mu\rho|v|}{h_{\rm p}}}\,. \tag{9}$$

For the parametrization of the interphasial heat exchange coefficient $\tilde{h}$ that appears in the energy equations (3) and (4), we employ the same reasoning. The heat transfer rate between the two phases inside the porous medium is approximated by the rate of steady-state heat transfer across the surface of a single cylinder multiplied by the number density of cylinders $N_{\rm c}$. This results in the following expression for $\tilde{h}$ in non-dimensional form,

$$\tilde{h} \;=\; \frac{4(1-\phi)}{d_{\rm c}^2}\overline{Nu}_{d_{\rm c}}\frac{k}{RePr}\,. \tag{10}$$

In this relation, the Reynolds and Prandtl numbers are based on the macroscopic reference values, whereas $\overline{Nu}_{d_{\rm c}}$ is the Nusselt number at the scale of the porous microstructure, averaged over the surface of a single element of the solid matrix. Herein we employ the widely used empirical correlation for $\overline{Nu}_{d_{\rm c}}$, provided in [13] for $Pr \geq 0.7$.

$$\overline{Nu}_{d_{\rm c}} \;=\; CRe_{\rm d_c}^{m}Pr^{1/3}\,, \tag{11}$$

where C and m depend on $Re_{d_{\rm c}}$ and their values are given in [13].

The algorithm for the numerical treatment of the governing system of equations (1)-(4) is based on a predictor-corrector time-marching scheme and incorporates a projection method for the computation of the pressure field [14]. It is an extension of the single-phase flow solver [15] to domains with superimposed porous and pure-fluid domains. The time integration of the convective and diffusive terms in the momentum and energy equations (2)-(4) is performed via an Adams–Bashforth method in the predictor stage and via a Crank–Nicholson method in the corrector stage. A projection method is then used for the computation of the dynamic pressure, i.e. by taking the divergence of (2). In this manner we obtain an elliptic equation that is solved numerically using a GMRES solver [16] implemented in the library PETSc [17, 18]. This library was also used in order to parallelize the algorithm. Once the pressure field is known, the velocity field is computed directly from (2). Spatial discretization of the equations is performed with 2nd-order differences on a collocated grid system. This is combined with a flux interpolation technique to avoid the pressure odd-even decoupling that is typically encountered when using such grids as in [15, 19].

3. NUMERICAL SETUP

The flow domain is a rectangular parallelepiped of size $\hat{h}_{\rm r} \times (\hat{h}_{\rm p} + \hat{h}_{\rm r}) \times \hat{h}_{\rm r}$ where $\hat{h}_{\rm r}$ is the characteristic length and $\hat{h}_{\rm p}$ the height of the porous region. As shown in Figure 1, the porous region is also a rectangular parallelepiped immersed in the flow domain. It is centered along the centerline of the flow domain and its dimensions are $\hat{l}_{\rm p} \times \hat{h}_{\rm p} \times \hat{l}_{\rm p}$. In this study, the porous region extends at 90 % of the length and width of the flow domain, *i.e.* $\hat{l}_{\rm p} = 0.90\ \hat{h}_{\rm r}$. As mentioned, we use the height of the pure-fluid domain $\hat{h}_{\rm r}$ as the reference length and its value is equal to 1.77 cm. Also, the height-to-width ratio is taken equal to one, whereas the height of the porous region $\hat{h}_{\rm p}$ is equal to 0.2 $\hat{h}_{\rm r}$. Thus, the overall height of the computational domain is equal to 1.2 $\hat{h}_{\rm r}$. This brings the total height of the domain to 2.13 cm. Of course, this value does not correspond to the actual depth of a SFP but herein we are interested in the modeling aspects of SFPs and in providing physical insight about free convection above heated porous media.

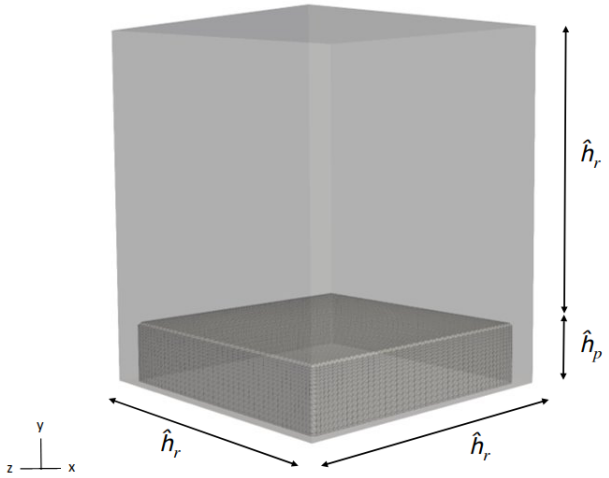


Figure 1. Illustration of the computational domain with the immersed porous region. The dimensions of the computational domain are $\hat{h}_\mathrm{r} \times (\hat{h}_\mathrm{p} + \hat{h}_\mathrm{r}) \times \hat{h}_\mathrm{r}$ and those of the porous region are $\hat{l}_\mathrm{p} \times \hat{h}_\mathrm{p} \times \hat{l}_\mathrm{p}$. The top wall is kept at constant temperature $\hat{T}_\mathrm{c}$. Also, $\hat{T}_\mathrm{h}$ stand for the area-averaged temperature at the top of the porous region in the fully developed flow.

Table I. Reference temperature $\hat{T}_\mathrm{r}$, temperature difference $\Delta\hat{T}$, density $\hat{\rho}_\mathrm{r}$, thermal expansion coefficient $\hat{\beta}_\mathrm{r}$, kinematic viscosity $\hat{\nu}_\mathrm{r}$, thermal conductivity $\hat{k}_\mathrm{r}$ and thermal diffusivity $\hat{\alpha}_\mathrm{r}$ of water.

$\hat{T}_\mathrm{r}$ [K]	$\Delta\hat{T}$ [K]	$\hat{\rho}_\mathrm{r}$ $[kg/m^3]$	$\hat{\beta}_\mathrm{r}$ $[1/K]$	$\hat{\nu}_\mathrm{r}$ $[m^2/s]$	$\hat{k}_\mathrm{r}$ $[W/mK]$	$\hat{\alpha}_\mathrm{r}$ $[m^2/s]$
293.15	8.92	997.14	2.30×10^{-4}	9.03×10^{-7}	0.607	1.45×10^{-7}

For the problem at hand, thermal convection is driven by the heat released by the solid matrix. The distribution of this heat source is denoted by r. The temperature difference $\Delta\hat{T}$ is taken to be the difference between the mean temperature at the horizontal plane of the macroscopic interface, $\hat{T}_\mathrm{h}$ and the temperature at the top of the domain $\hat{T}_\mathrm{c}$ when the flow has become statistically stationary. In our simulation, $\hat{T}_\mathrm{c}$ is fixed and equal to 293.15 K and we obtain $\hat{T}_\mathrm{h} = 302.07$ K. The corresponding temperature difference is then $\Delta\hat{T} = 8.92$ K. The reference temperature is defined as $\hat{T}_\mathrm{r} = \frac{\hat{T}_\mathrm{h}+\hat{T}_\mathrm{c}}{2}$ $\hat{T}_\mathrm{r}$ and is equal to 297.61 K. Finally, the material properties at $\hat{T}_\mathrm{r}$ are used as reference values for non-dimensionalization purposes. These are provided in Table I.

In thermal convection, the pertinent dimensionless groups are the height-to-width ratio of the flow domain, the Prandtl number, and the Rayleigh number which is defined as

$$Ra = \frac{\hat{g}\hat{\beta}_\mathrm{r}\hat{h}_\mathrm{r}^3\Delta\hat{T}}{\hat{\nu}_\mathrm{r}\hat{\alpha}_\mathrm{r}}. \tag{12}$$

It is worth noting that to allow comparisons with classical Rayleigh-Bénard Convection (RBC), we use the height of the pure-fluid domain $\hat{h}_\mathrm{r}$ in the definition of Ra.

The free-fall velocity $\hat{u}_\mathrm{r} = \sqrt{\hat{\beta}_\mathrm{r}\hat{g}\hat{h}_\mathrm{r}\Delta\hat{T}}$ and free-fall time $\hat{t}_\mathrm{r} = \hat{h}_\mathrm{r}/\hat{u}_\mathrm{r}$ are the reference velocity and time unit, respectively. The values of the dimensionless numbers of the problem (*i.e.* the Rayleigh Ra, Prandtl Pr, Reynolds Re and Richardson Ri numbers) are also provided in Table II.

Table II. Free-fall velocity $\hat{u}_{\mathrm{r}}$, free-fall time $\hat{t}_{\mathrm{r}}$, Rayleigh Ra, Prandtl Pr, Reynolds Re and Richardson numbers Ri for the two heat source distribution considered herein.

$\hat{u}_{\mathrm{r}}$ [m/s]	$\hat{t}_{\mathrm{r}}$ [s]	Ra	Pr	Re	Ri
0.019	0.94	8.63×10^5	6.21	372.76	486.45

Table III. Dimensionless values of the parameters of the solid matrix at the reference temperature $\hat{T}_{\mathrm{r}}$, non-dimensionalized by the corresponding reference values.

d_{c}	ρ_{s}	k_{s}	c_{ps}
0.001	7.92	21.38	0.122

The total power $\hat{Q}$ supplied to the solid is assumed to be 0.37 W. Since we consider uniform heat-source distribution, then the source term r in the energy equation of the solid matrix (4) is equal to the ratio between $\hat{Q}$ and the volume of the solid matrix. The resulting dimensionless value is $r = 0.00082$.

Concerning the physical parameters of the porous medium, we assume that the (dimensionless) diameter of the cylindrical elements of the solid matrix, d_{c}, is equal to 0.001. Also, the cylinders are assumed to be made of stainless steel. Their dimensionless thermo-physical properties are listed in Table III.

Since the boundaries of the computational domain are solid walls, the no-slip kinematic condition is prescribed at all of them. Concerning the thermal boundary conditions, the bottom and side walls are assumed to be adiabatically isolated, whereas the temperature at the top wall is fixed at T_{c} where $T_{\mathrm{c}} = \hat{T}_{\mathrm{c}}/\hat{T}_{\mathrm{r}}$ is the non-dimensional cold temperature. As mentioned above, equations (1)-(3) being valid in both the porous and the pure-fluid regions, there is no need for supplementary matching conditions at the macroscopic interface for the variables associated with the fluid phase. However, the energy balance law for the solid matrix (4) is valid only in the porous region. Therefore it should be supplemented with a condition at the interface. In our study, we prescribe the condition proposed in [8], namely,

$$(1-\phi)(\mathbf{k}_{\mathrm{s}}\nabla T_{\mathrm{s}})\cdot\tilde{\mathbf{n}} \;=\; 0\,, \qquad \text{at } S_\Omega. \tag{13}$$

where $\tilde{\mathbf{n}}$ is the unit vector normal to the interface.

Finally, since our study consists of direct numerical simulations in the pure-fluid region, the computational grid should be sufficiently refined so as to ensure that all flow scales in this region are resolved. This is achieved by employing certain resolution criteria for boundary-layer regions and the bulk of the pure-fluid domain [20]. More specifically, we invoke the universal criterion of [21] for the minimum number of cells in the hydrodynamic and thermal boundary layers, $N_{\mathbf{u}}$ and N_θ respectively (see Table IV). Also, in the bulk of the domain in the bulk, the cell size must be at the order of the Kolmogorov and Corssin scales of the flow turbulence [22]. We recall that the Kolmogorov scale is the size of the smallest turbulent eddies in the flow and the Corrsin scale represents the relevant microscale of thermal fluctuations. The size of the largest computational cell should be smaller than both of these scales. Then, once the minimum resolution requirements are set, a hyperbolic-tangent expansion function is employed to stretch the mesh from the smallest cells at the boundaries to the largest ones in the bulk of the domain. The number of cells in the three spatial directions and the number of cells used for the discretization of the hydrodynamic and thermal boundary layers are provided in Table IV.

Table IV. Grid resolution. N_x, N_y, and N_z are the number of cells in the x, y, and z directions respectively. N_{u} and N_θ are the number of cells in the hydrodynamic and thermal boundary layers respectively. The numbers in parentheses correspond to the minimum resolution requirements according to [21].

N_x	N_y	N_z	N_{u}	N_θ
50	65	50	6 (4)	3 (2)

With regard to the time-step of the simulations, the Courant number is set equal to 0.08 for purposes of numerical stability. This constraint on the time-step is stricter than that of the Kolmogorov and Corrsin timescales; it is therefore assumed that the smallest timescales of the flow are well captured.

Finally, as regards the initial conditions, we assume that the fluid is initially at rest and that its temperature is equal to the cold temperature T_{c} in the entire computational domain. In the porous region, the solid matrix is also initialized at the same temperature T_{c}.

4. NUMERICAL RESULTS

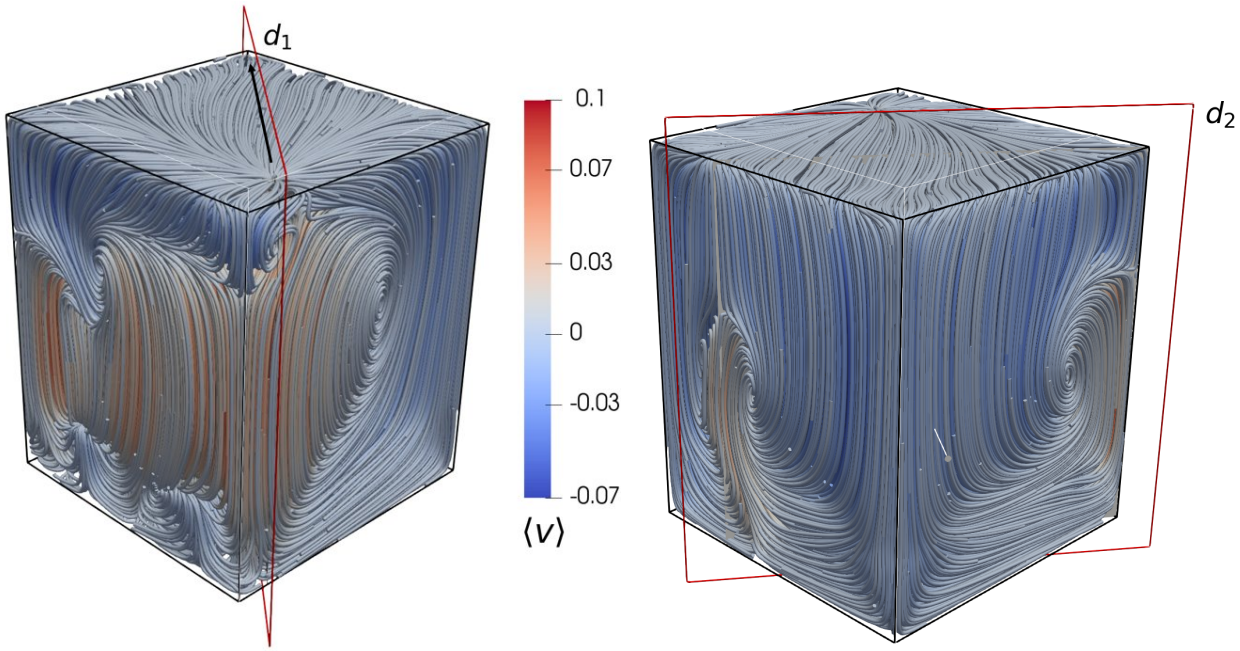
In this section, we present numerical results for the setup considered in our study. We start the simulation with the initial conditions described above and let the flow develop. After a while, turbulent structures begin to form. Eventually, the flow becomes statistically stationary (fully developed) and the area-averaged temperature T_{h} assumes a constant value. According to our simulations, it takes approximately 1000 free-fall times for the flow to become fully developed. Afterward, time averages are taken over a period of 200 free-fall times for purposes of statistical analysis. Below we present results in terms of the normalized temperature θ, defined as

$$\theta = \frac{\hat{T} - \hat{T}_{\mathrm{r}}}{\Delta \hat{T}}, \qquad \theta_{\mathrm{s}} = \frac{\hat{T}_{\mathrm{s}} - \hat{T}_{\mathrm{r}}}{\Delta \hat{T}} \tag{14}$$

where $\hat{T}$ and $\hat{T}_{\mathrm{s}}$ are the temperature of the fluid and the solid respectively.

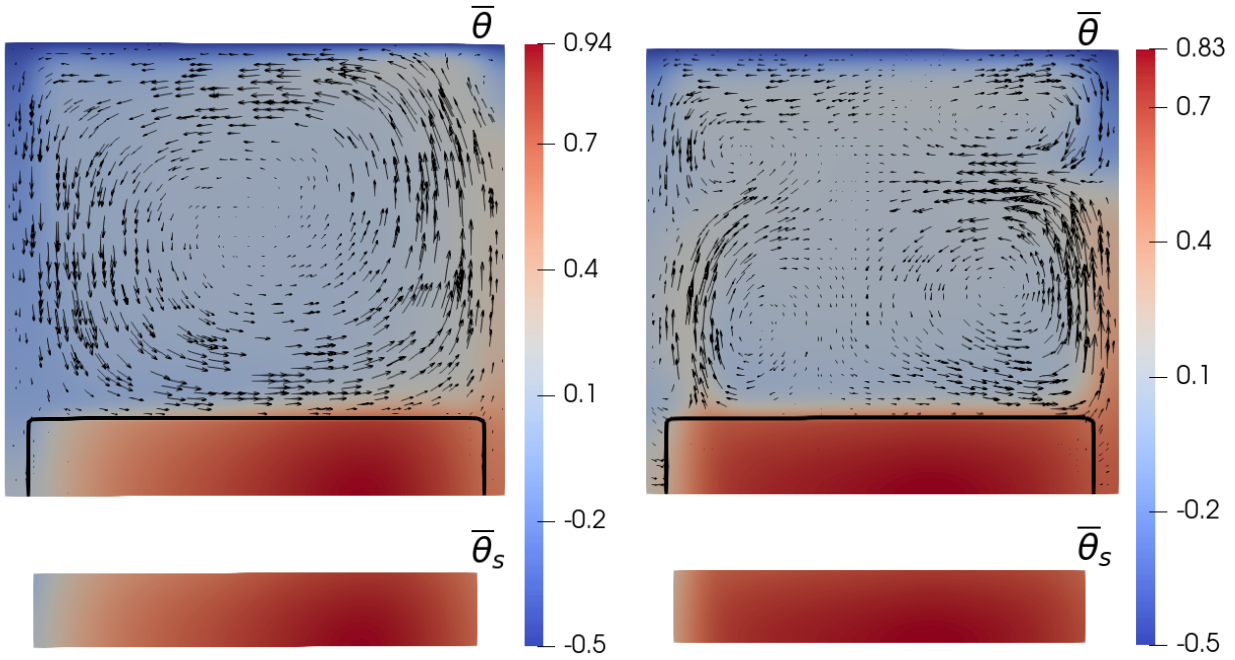
In Figures 2a and 2b, we present plots of the time-averaged streamlines colored by the mean vertical velocity. These figures help to qualitatively visualize the flow patterns. According to these plots, a Large-Scale Circulation (LSC) is formed that extends through the entire pure-fluid region. Typically, in RBC, the LSC is aligned with one diagonal plane. In this case, however, as shown in Figure 2a, the impingement point of the LSC at the top wall is not located at the neighboring diagonal plane but has a certain offset from it. Nonetheless, the bottom impingement point (not shown) is located at the opposite corner and at height $y = h_{\mathrm{p}}$. The vertical plane passing by the two impingement points will henceforth be denoted by d_1. Also, in Figure 2a some intricate recirculation patterns can be seen in the region between the wall and the porous medium. Moreover, the streamlines of Figure 2b reveal two large vortical structures at the front faces of the computational domain. The first one is located close to its neighboring edge, whereas the left one is located closer to the bulk. By contrast, in RBC both vortices are situated close to their corresponding neighboring edge. Accordingly, the vertical plane passing by the "centers" of these two vortices is denoted as d_2.

Color plots of the normalized time-averaged temperatures for the two phases at those two planes (d_1 and d_2) are provided in Figures 3a and 3b. Further, the color plot of the fluid temperature is superimposed with the corresponding in-plane velocity vectors. In Figure 3a, we can infer the upward motion of water at the left edge and its downward motion at the right edge. These streams of opposite directions are part of the Large



(a) **(b)**

Figure 2. Time-averaged streamlines colored by mean vertical velocity.



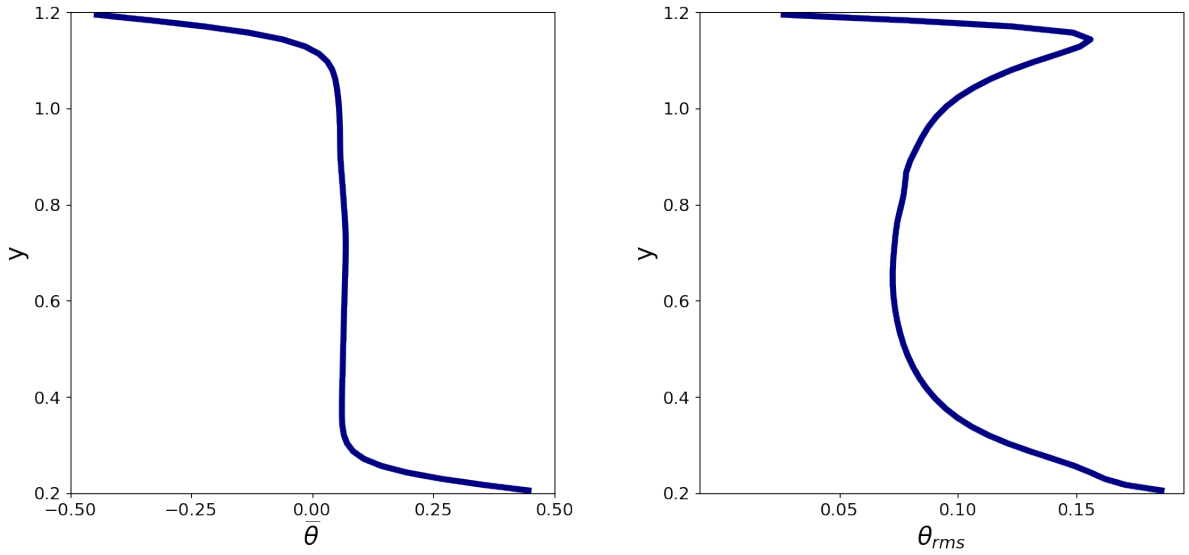
(a) **(b)**

Figure 3. Color plots of the normalized time-averaged temperature of the fluid (up) and the solid (down) with superimposed in-plane velocity vectors: (a) at the plane d_1 and (b) at the plane d_2.

Scale Circulation (LSC) that extends through the entire plane. A smaller recirculation zone can also be seen at the top right corner of the plane d_1. A similar flow structure is observed in turbulent RBC too. In the same

figure, we can further observe the horizontal motion of fluid above the porous medium, which is also part of the LSC. Then a shear layer is developed at the macroscopic interface due to the large difference between the horizontal velocities above and inside the porous medium.

We also note that although the heat source distribution is uniform, neither the temperature of the solid matrix nor that of the interstitial fluid are uniform in the porous region. Instead, a horizontal temperature gradient is present in the temperature field of both phases. This can be explained by the fact that the LSC passes over and through the macroscopic interface and thereby inducing this horizontal temperature gradient. In Figure 3b, we can notice two pairs of asymmetric counter-rotating vortices. Again, this behavior contrasts with the symmetric pairs of counter-rotating vortices that are usually seen in turbulent RBC. This asymmetry is due to the absence of a hydrodynamic boundary layer at the pure fluid - porous medium interface which allows for higher horizontal velocities. Further, by comparing the phasial temperature profiles in Figures 3a and 3b, we can see that the peak temperature at the plane d_1 is higher than at the plane d_2. In other words, the horizontal thermal convection in the porous region is stronger at d_1 than at d_2. This is due to the fact that the horizontal fluid motion induced by the LSC is stronger than that induced by the pairs of vortices shown at plane d_2.

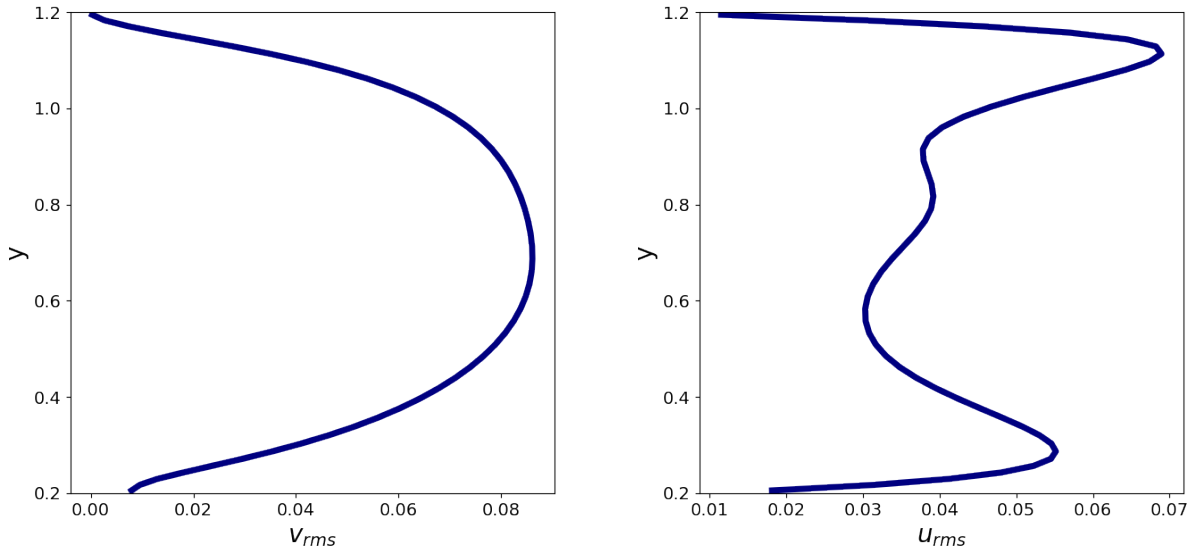


(a) **(b)**

Figure 4. (a) Mean area-averaged across the vertical direction temperature, $\bar{\theta}$, mean temperature rms area-averaged, θ_{rms}.

Next, we examine the first and second-order statistics of the velocity and temperature fields in the pure-fluid domain, i.e. for $y > 0.2$. In Figure 4a, we plot the graph for the area- and time-averaged normalized temperature along the vertical axis. Contrary to the corresponding RBC, the temperature in the bulk is not the mean of the hot and cold temperatures. Instead, the mean temperature profile is shifted towards the temperature θ_{h}. The plot of the root-mean-square (rms) of that normalized temperature is shown in Figure 4b. Therein, we first observe one peak at the top boundary due to the thermal boundary layer. Then the profile drops in the bulk as is usual in turbulent convection. Afterward, in the vicinity of the pure fluid-porous medium interface, the temperature fluctuations increase again and attain a peak right at the interface. This peak can be explained by the shear layer that develops at the interface which enhances the thermal

mixing.



(a) **(b)**

Figure 5. Area-averaged velocity rms: (a) Vertical velocity rms, v_{rms} , and (b) in-plane velocity rms, u_{rms}.

The rms plots of the vertical and horizontal velocities are shown in Figure 5a and 5b respectively. The horizontal velocity fluctuations are defined as,

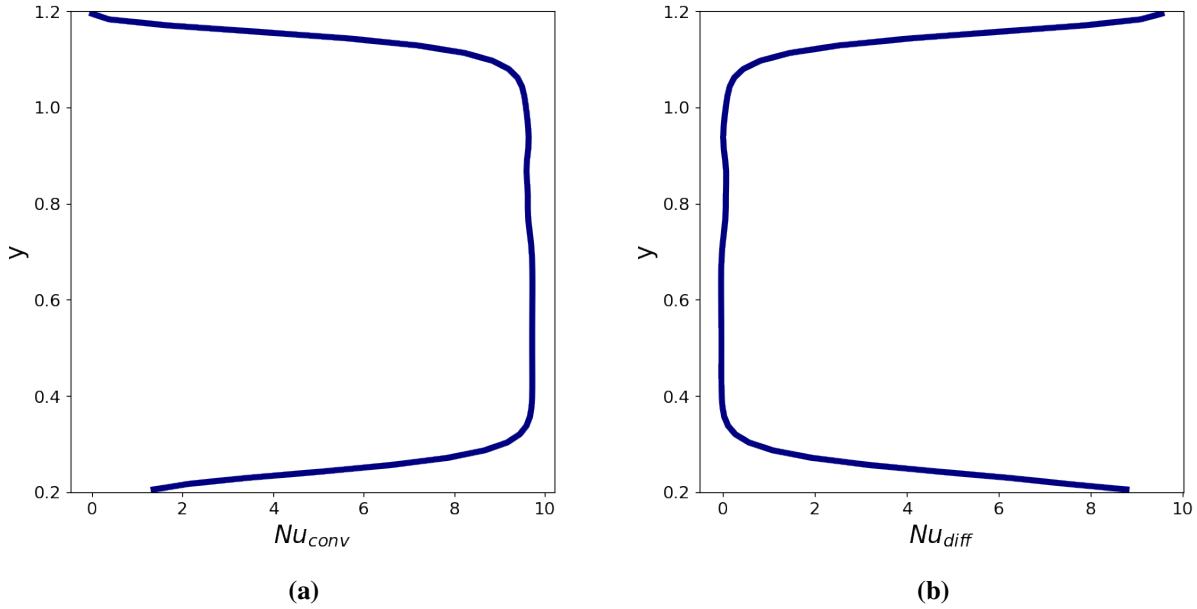
$$u_{\mathrm{rms}} = \sqrt{\langle u'^2 + w'^2 \rangle}_{xz} . \tag{15}$$

For v_{rms}, the observed parabolic profile shows zero v_{rms} values at the top boundary which rises toward a maximum value in the bulk as usual. Moreover, this peak value has the same order of magnitude as equivalent RBC. The profile then drops up to 0.01 at the macroscopic interface. It is interesting to note that as opposed to RBC, v_{rms} does not vanish at the interface since some fluid is moving from and to the porous region. Concerning Figure 5b, we identify two local peaks at the top boundary and the macroscopic interface, as it is also the case in turbulent RBC. Nonetheless, two main differences are noticed. Firstly, the peak at the top is higher, which is due to the hydrodynamic boundary layer at the top wall. Secondly, u_{rms} does not vanish at this interface, which is due to the shear layer therein.

Finally, we present results for the Nusselt number. To obtain a global estimation, we first introduce the local Nusselt number Nu_{y} as in [23],

$$Nu_{\mathrm{y}} = \underbrace{\sqrt{RaPr}\,\langle \rho v \theta \rangle_{xzt}}_{Nu_{\mathrm{conv}}} - \underbrace{\langle k \frac{\partial \theta}{\partial y} \rangle_{xzt}}_{Nu_{\mathrm{diff}}} . \tag{16}$$

In Figure 6a and 6b, we provide plots of the convective and diffusive components of the local Nusselt number, respectively. We can see that both components are almost constant in the bulk of the pure-fluid region. In Figure 6a we infer that the convective component is negligible at the top boundary but not



(a) **(b)**

Figure 6. Plots of the time- and area-averaged components of Nusselt over the vertical axis. (a) Convective part of the Nusselt number Nu_{conv} (b) Diffusive part of the Nusselt number Nu_{diff} .

at $y = h_{\mathrm{p}}$ as the flow is also convected through the interface. The opposite holds true for the diffusive component whose plot is provided in Figure 6b. The time and volume-averaged (global) Nusselt number, Nu, is computed by averaging Nu_{y} in the y-direction. In our simulation, the predicted value of the global Nusselt number Nu is 9.7. By using the correlation $Nu = 0.124Ra^{309}$ proposed in [24] for classical RBC to obtain the Rayleigh number corresponding to a Nusselt number of 9.7, we get a corresponding $Ra = 1.3 \times 10^6$. This means that in classical RBC, the Rayleigh number required to have the same amount of convection as our simulation at $Ra = 8.63 \times 10^5$ is a higher Rayleigh number equal to 1.3×10^6.

5. CONCLUSIONS

We have developed a new parallel algorithm for time-accurate three-dimensional simulations in domains with porous and pure-fluid regions. Based on this algorithm. we have performed simulations of turbulent thermal convection over and through an internally heated porous medium. According to the configuration employed in our study, the Rayleigh number in the pure-fluid region reaches $Ra = 8.6 \times 10^5$. This results in moderately turbulent thermal convection, which is nonetheless more intense than the corresponding RBC case. As the flow develops, an LSC extending through the entire pure-fluid region is formed. However, in contrast to RBC, the LSC is not aligned to one of the two diagonal planes but is, instead, tilted with respect to them. Interestingly, the LSC induces a horizontal temperature gradient inside the porous region for both phases (fluid and solid matrix). Further, the second-order statistics are asymmetric with respect to the mid-height of the pure-fluid region which is a clear deviation from the classical RBC. This is due to the shear layer that develops at the interface between the pure fluid and the porous medium. Finally, our simulation predicts a Nusselt number that is 1.5 times that of the equivalent RBC. In other words, the heated porous medium enhances convection considerably.

ACKNOWLEDGMENTS

The first author gratefully acknowledges the financial support of the National Research Fund of Belgium (FNRS) in the form of a FRIA fellowship. The second author acknowledges the financial support provided by the Belgian Federal Ministry of Energy under the Energy Transition Fund, project SFP-LOCA. Further, the authors would like to thank the team of PETSc for their support concerning the PETSc software library.

REFERENCES

1. OECD (Nuclear Energy Agency), "Phenomena Identification and Ranking Table, R&D Priorities for Loss-of-Cooling and Loss-of-Coolant Accidents in Spent Nuclear Fuel Pools," (2018)
2. J. A. Ochoa-Tapia and S. Whitaker, "Momentum transfer at the boundary between a porous medium and a homogeneous fluid—I. Theoretical development," *Int. J. Heat Mass Tran.*, **38** (14), pp. 2635–2646 (1995)
3. K. Vafai, *Handbook of Porous Media*, Crc Press (2015)
4. S. C. Cowin, *Continuum Mechanics of Anisotropic Materials*, Springer Science & Business Media (2013)
5. P. D. Antoniadis and M. V. Papalexandris, "Dynamics of shear layers at the interface of a highly porous medium and a pure fluid," *Phys. Fluids*, **27**, pp. #014104 (2015)
6. M. V. Papalexandris, "'A two-phase model for compressible granular flows based on the theory of irreversible processes," *J. Fluid. Mech.*, **517**, pp. 103–112 (2004)
7. C. Varsakelis and M. V. Papalexandris, "The equilibrium limit of a constitutive model for two-phase granular mixtures and its numerical approximation," *J. Comput. Phys.*, **229** (11), pp. 4183–4207 (2010)
8. M. V. Papalexandris and P. D. Antoniadis, "A thermo-mechanical model for flows in superposed porous and fluid layers with interphasial heat and mass exchange," *Int. J. Heat Mass Tran.*, **88**, pp. 42–54 (2015)
9. M. V. Papalexandris, "On the applicability of Stokes' hypothesis to low-Mach-number flows," *Continuum Mech. Therm.*, **32**, pp. 1245–1249 (2019)
10. W. Wagner and H. Kretzschmar, *International Steam Tables - Properties of Water and Steam based on the Industrial Formulation IAPWS-IF97*, Springer, Berlin, Germany (2019)
11. M. V. Papalexandris, "Attenuation of gaseous detonations by porous media of fine microstructure," *Combust Fl.*, **232**, pp. #111518 (2021)
12. D. L. Koch and A. J. Ladd, "Moderate Reynolds number flows through periodic and random arrays of aligned cylinders," *Journal of Fluid Mechanics*, **349**, pp. 31–66 (1997)
13. F. P. Incropera et al., *Fundamentals of Heat and Mass Transfer*, volume 6, Wiley New York (1996)
14. P. D. Antoniadis and M. V. Papalexandris, "Numerical study of unsteady, thermally-stratified shear flows in superposed porous and pure-fluid domains," *Int. J. Heat Mass Tran.*, **96**, pp. 643–659 (2016)
15. B. Lessani and M. V. Papalexandris, "Time-accurate calculation of variable density flows with strong temperature gradients and combustion," *J. Comput. Phys.*, **212** (1), pp. 218–246 (2006)
16. G. H. Golub and C. F. van Loan, *Matrix Computations*, JHU Press, fourth edition, (2013)
17. S. Balay et al., "PETSc Users Manual," ANL-95/11 - Revision 3.11, Argonne National Laboratory (2019)

18. S. Balay, W. D. Gropp, L. C. McInnes, and B. F. Smith, "Efficient Management of Parallelism in Object Oriented Numerical Software Libraries," *Proc. Modern Software Tools in Scientific Computing*, pp. 163–202, Birkhäuser Press, (1997)

19. B. Lessani and M. V. Papalexandris, "Numerical study of turbulent channel flow with strong temperature gradients," *Int. J. Numer. Method. H.*, **18**, pp. 545–556 (2008)

20. W. A. Hay and M. V. Papalexandris, "Evaporation-driven turbulent convection in water pools," *J. Fluid Mech.*, **904**, pp. A21 (2020)

21. O. Shishkina, R. J. Stevens, S. Grossmann, and D. Lohse, "Boundary layer structure in turbulent thermal convection and its consequences for the required numerical resolution," *New J. Phys.*, **12** (7), pp. 075022 (2010)

22. G. Grötzbach, "Spatial resolution requirements for direct numerical simulation of the Rayleigh-Bénard convection," *J. Comput. Phys.*, **49** (2), pp. 241–264 (1983)

23. W. A. Hay, J. Martin, B. Migot, and M. V. Papalexandris, "Turbulent thermal convection driven by free-surface evaporation in cuboidal domains of different aspect ratios," *Physics of Fluids*, **33** (1), pp. 015104 (2021)

24. J. Niemela, L. Skrbek, K. Sreenivasan, and R. Donnelly, "Turbulent convection at very high Rayleigh numbers," *Nature*, **404** (6780), pp. 837–840 (2000)